

High-mobility inchworm climbing robot for steel bridge inspection

Tzu-Hsuan Lin^{a,*}, Alan Putranto^{a,b}, Pin-Hang Chen^a, Yun-Zhen Teng^a, Li Chen^a

^a Department of Civil Engineering, National Central University, Taoyuan 32011, Taiwan.

^b Department of Civil Engineering, Ketapang State Polytechnic, Ketapang 78813, Indonesia.



ARTICLE INFO

Keywords:

Climbing robots
Bionics
Bridge inspection
Steel box girders
Steel diaphragms
3D printing
HMICRobot

ABSTRACT

The High Mobility Inchworm Climbing Robot (HMICRobot), capable of traversing diaphragms between sections and performing internal inspections of steel box girder bridges, was developed through our mechanical design combined with finite element simulations and adhesion force experiments. Compared to existing robots in the literature, the developed HMICRobot exhibits superior climbing and obstacle-crossing capabilities, benefiting from its hybrid power design, unique footpad electromagnetic control, and central core module with large-size wheels that provide stable and efficient mobility on both steel surfaces and the ground. The robot's exceptional locomotion capabilities, including vertical and horizontal climbing, 360-degree flipping, and obstacle crossing, make it a promising solution for complex inspection and maintenance tasks in steel box girders. In the field of inspection robots, the HMICRobot represents a significant advancement, especially for performing internal inspections of steel box girder bridges.

1. Introduction

Bridges need regular inspection and maintenance to ensure safety. However, inspections can be challenging due to a lack of safe access points, high altitude operations, difficult transportation, or narrow structure spaces. This puts engineers at risk when they have to climb onto the bridge structure to perform inspections and maintenance work. A mobile unmanned vehicle that combines robotics and inspection instruments has been proposed to address this issue and improve inspection efficiency. This system would allow for safe, non-invasive inspections while reducing risks to human inspectors.

Various solutions have been proposed in the field of robotic bridge inspection. An automatic bridge inspection robot has been proposed that can arrange tasks in advance, customize the navigation route, and automatically build a 3D point cloud of the bridge [1]. However, the effectiveness of this solution can be limited because it relies on manually created inspection plans. Many studies have combined robots with Nondestructive Testing (NDT) technology to address this limitation. For example, a bridge deck inspection system that integrates multiple NDT sensors and navigation control algorithms has been developed to enable the robot to accurately and autonomously maneuver on the bridge deck to collect visual images and conduct NDT measurements [2]. Additionally, a robot system that integrates ground penetrating radar (GPR) and electrical resistivity (ER) has been developed for real-time, efficient

bridge deck inspection [3].

Some studies have integrated cameras and Lidar into inspection robots to improve inspection accuracy and efficiency. These robots use a 3D model of the space, measured in advance with Lidar, along with Simultaneous Localization and Mapping (SLAM) technology and the Robot Operating System (ROS) for data collection, communication, and navigation during actual bridge inspections [4]. Research also proposed an automatic mechanical detection and mapping robot system for crack detection [5]. The robot is equipped with a camera to collect images on the bridge deck, and a path-planning algorithm based on genetic algorithms is developed to ensure that the robot can collect all images on the bridge deck. NDT is used to detect vertical cracks, and the Extended Kalman Filter (EKF) is used to fuse various data from different sources to solve the problem of reduced positioning accuracy due to moving objects.

Climbing robots have been proposed to inspect bridge components that are difficult to reach. By using these robots to access cables, joints, and hangers, bridge maintenance can be performed more efficiently and safely, reducing the risks associated with manual inspection methods. While previous research has primarily focused on using robots on bridge decks for inspection purposes [2], there is a need for robots that can access more complex steel bridge environments. To meet this need, researchers have developed climbing robots that can attach to steel surfaces using permanent magnets and tracks, allowing them to crawl on

* Corresponding author.

E-mail address: cornetlin@gmail.com (T.-H. Lin).

surfaces covered in bolts [6,7].

Additionally, suction cup climbing robots have been developed to automate the data collection process for inspecting various types of infrastructure, including bridges, tunnels, dams, and building facades. These robots can identify cracks on concrete walls using a neural network [8]. Steel structure climbing robots have also been developed that use the adhesive force generated by permanent magnets and flexible magnetic arrays in different modes to overcome obstacles such as nuts and bolts [9,10].

When it comes to inspecting more complex steel bridge environments, some bio-inspired climbing robots have been developed, such as climbing robots with four claws that can extend outward and slide on the tips of hooks to find stable points and grip onto rough walls, enabling the robot to adapt to uneven and rough surfaces [11]. Another example is a centipede-like robot with an algorithm for navigating between bridges, although it is currently limited to simulation [12]. Additionally, robots with similar mechanical designs have been used for climbing steel bridges [13]. These innovative climbing robot designs offer a promising approach to inspecting more challenging components of bridges, such as cables, joints, and hangers, which are typically difficult to reach with manual inspection methods.

The research on climbing robots is an expanding field [14], and a comprehensive literature review was conducted to find an appropriate robotic platform for defect inspection [15]. Climbing robots for steel structures are based on magnetic adsorption and can be divided into three main types, permanent magnets, electromagnets, or hybrid magnets. Robots designed for steel trusses sometimes use retractable grippers to achieve climbing action via clamping and releasing [16]. These robots can have different forms and climbing mechanisms, including crawler robots [6], wheeled robots [17,18], and multi-legged robots, with two to eight feet being the most common [19]. For example, the bipedal PAMR1 robot, developed in 2000 [20,21], was designed with the understanding that the more limbs a robot has, the greater its payload capacity. However, too many limbs would become redundant regarding degrees of freedom (DOF), reducing a robot's compactness and efficiency. The six-legged REST robots can climb on vertical and horizontal magnetic surfaces with payloads of up to 100 kg [22]. Each foot on the REST robot has a magnetic switch device composed of a permanent magnet and an electromagnet, which allows the foot to support around 50% of the robot's total weight, regardless of the slope angle. Additionally, some scholars proposed the concept of an Omni-climber bipedal climbing robot that combines omnidirectional wheels [23,24]. However, it was not designed for steel bridge structures but specifically for arc-shaped pipe surfaces.

The concept of bionics has been a popular approach in the design of climbing robots, with the "inchworm" bipedal climbing robot being a commonly discussed format. Scholars have developed bipedal permanent-magnet climbing robots with a three-link articulation mechanism and a locking device at the end, utilizing this concept [25]. The locking device is composed of three magnetically switchable devices fixed to a frame, each equipped with a servo motor, a geared connection to the permanent magnet, and a pressure sensor for adhesion control. By rotating the gear, the device can be separated from the surface. Such robots require at least six DOF to reach all areas in their workspace.

Numerous robots based on the inchworm pattern have been developed, focusing on lightweight design, stability, increasing carrying capacity, and improving slow movement speed. Some robots use batteries, while others are connected to external power sources. For instance, the iCrawl is a small bionic robot with five DOF and a sensor under the adsorption device to ensure safe movement in any workspace and correct coordination. It is powered by a battery and has proven effective in climbing structures for inspection purposes [25]. Recent breakthroughs in climbing robot design have integrated a robot's magnetic-attraction device into a complex magnetic wheel mechanism. This new design allows the robot to walk on free vertical surfaces of steel bridges at a significantly improved speed. Incorporating a high-torque servo motor

enables the robot to switch between different planes while its 3D camera and Lidar maintain good directivity and reduce perceived vibration when rolling or crawling [26,27].

A new type of climbing robot, Eciton Robotica, has been developed and is similar to a reconfigurable soft robot [28,29]. Inspired by the cooperative movement of army ants, its self-assembling module enables this robot's body to include amorphous and adaptive mechanisms. Another novel design, especially for steel-structure inspection, is known as a roller chain-like robot [30]. Unlike most existing climbing robots, it can operate smoothly on various steel surfaces.

In addition to common climbing robots, unique climbing robots have been developed for steel cable and wall inspections. For instance, a climbing robot with an integrated quadrilateral independent suspension system has been developed for steel cable inspections on cable-stayed bridges. This robot has good adhesion and strong obstacle-crossing ability, making it well-suited for inspection on cable-stayed bridges. It comprises two climbing modules with power wheels connected along the steel cable. One climbing component belongs to the active climbing module, and the other to the passive climbing module. This robot also has a flexible quadrilateral independent suspension system that allows it to deform over a more extensive range of motion [31].

Another climbing robot designed for steel cable inspection imitates the motion of monkeys and is operated using a palm-based gripping system. This robot has two gripping modules connecting to its sliding module, allowing it to climb on the steel cable. The palm-based climbing robot requires fewer suitable footholds and can efficiently avoid obstacles attached to the surface of the steel cable, making it more efficient compared to a robot that climbs using wheels. Additionally, when moving in terrain with obstacles, the advantage of palm movement is more pronounced [32]. Another robot has been developed consisting of three rubber wheels connected by a support plate and springs. This robot achieves cable adhesion based on the relative rotation of the swing plate and the support plate, the scaling of the spring, and the adjustment of the distance between the rolling wheels. However, this type of robot is limited to steel cables or cylindrical structures [33].

Robots based on flight and propeller thrust have been developed for wall-climbing inspections. For instance, an unmanned aerial vehicle (UAV) system has been proposed for wall-climbing robots, in which the propulsion system used for the flight can be used as a thrust against the wall, converting the force into friction for adhesion or movement on the wall surface [34]. Propeller thrust wall-climbing robots can move forward or backward and adhere to the wall based on the reverse thrust of the propeller. The motor adjusts the angle of the rotor, and the rotor is fixed to the front and rear moving platforms, making the robot insensitive to the contact medium and surface characteristics [35]. However, this type of robot is only suitable for surface inspection of structures. Additionally, the lightweight of the robot can be easily affected by strong winds during the inspection, making it challenging for practical applications.

Despite the increasing development of inspection robots, most of the robots proposed in the literature are limited to climbing and inspecting the surface of structures. Few can overcome diaphragms between sections in the complex maintenance spaces inside the steel box girder bridges. Notably, the interior of steel box girders is typically separated by diaphragms, thin plates perpendicular to the ground, as shown in Fig. 1. This study aims to develop a climbing robot that can successfully traverse between diaphragm sections and comprehensively inspect the complex environment on the inner side of steel box girders. In this work, an innovative mechanical structure and operating mechanism have been designed and implemented to develop a prototype robot. Additionally, finite element simulations of primary component materials were conducted, and the adhesion force was measured and analyzed experimentally. Finally, a simulated inspection was carried out using an L-shaped thin steel plate as a model for the diaphragms to demonstrate the climbing capability of the developed robot.



Fig. 1. Internal inspections of steel box girder bridges and the diaphragms that separate various sections of the bridge.

2. Design of high-mobility inchworm climbing robot

2.1. Mechanical structure and functions

The HMICRobot was developed to create an inspection robot that could conduct internal inspections of steel box girder bridges and traverse the diaphragms that separate various sections of the bridge. Fig. 1 illustrates an internal inspection of steel box girder bridges and the diaphragms that separate various bridge sections. The HMICRobot was based on the inchworm and simulated its physiological structure and movement. The robot's morphology and climbing behavior were worm-

like, with footpads on both the left and right extremities. Its footpad design, derived from the inchworm's tentacles, allowed the robot to cling to the contact surface and climb. It also had the ability to bend its body or use a one-legged cantilever to reach a desired location in space. The robot's mechanical structure was lightweight and compact, with a hybrid power design, a unique footpad electromagnetic control, and a central core module with large-size wheels that provided stable and efficient mobility on both steel surfaces and the ground. The robot's exceptional locomotion ability included the capability of climbing vertically and horizontally, as well as performing 360-degree flipping and obstacle-crossing, making it a promising solution for conducting complex inspections and maintenance tasks in steel box girders.

Fig. 2 (a) shows the 3D design of the HMICRobot, where the components, including links, joints, and modules, are labeled with numbers (See Table 1). The robot weighs 9945 g and has dimensions of 726.8 mm (length) x 272.1 mm (width) x 154.9 mm (height). Fig. 2(b) shows that the robot is designed with a six-degree-of-freedom mechanism consisting of five members labeled L1 to L5 and six movable joints labeled J1 to J6. Each J1 through J4 is equipped with a servo motor with a range of motion limited to $\pm 120^\circ$ degrees to prevent self-collision during deformation. The servo motors at J1 and J6 rotated the footpad around its axis, with the range of motion also limited to $\pm 120^\circ$ degrees. A 90-degree gear moves servo motors to the side by its rotating mechanism, shortening the length between L1 to L5 and the footpad.

Regarding material selection, 90% of the components were made of 6061 aluminum alloy, while non-structural components were made of general-purpose PLA material. Finite element analysis was performed on three members (L1, L2, and L3) that were susceptible to deformation.

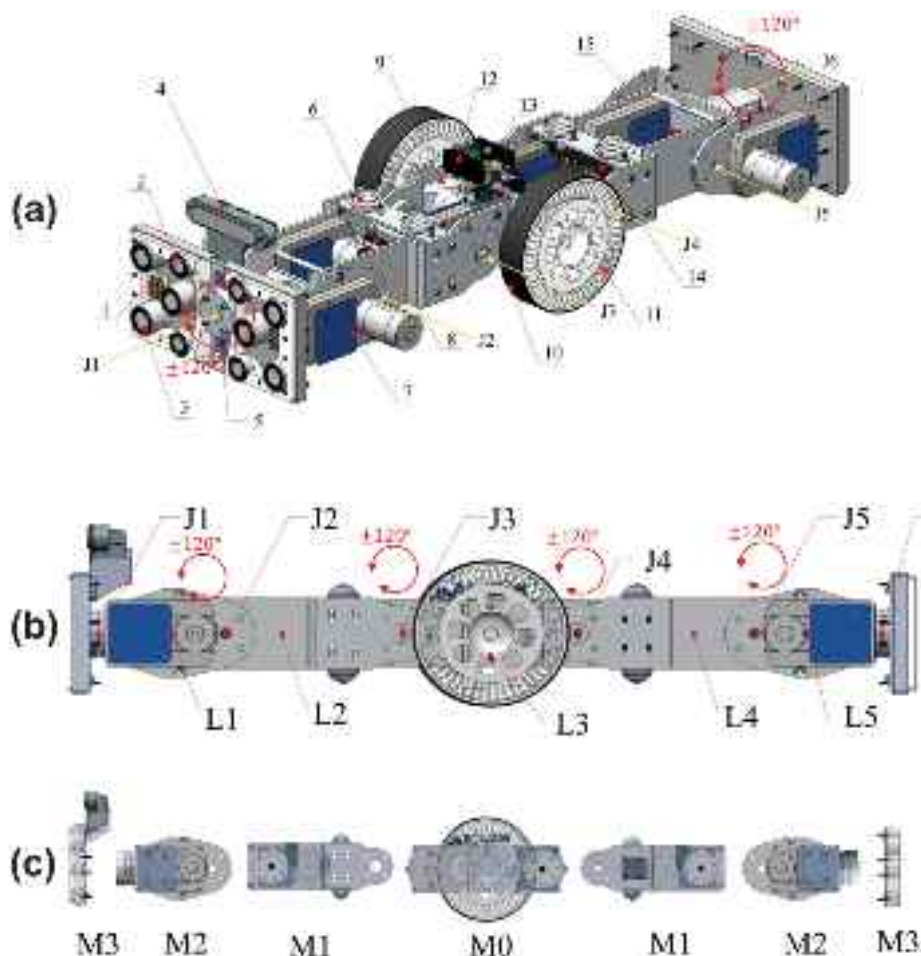


Fig. 2. (a) HMICRobot 3D model with component configuration; (b) Link and joint positions; (c) Defined Modules.

Table 1
Annotated HMICRobot component list.

No.	Unit	Component	Description
1	4	SMD 5050 LED	Lighting device (voltage: DC12V; power: 1.92 W)
2	8	DSD2510 electromagnet	Magnetic adhesion (voltage: DC12.5 V; power: 43.7 W)
3	12	DX3021 electromagnet	Pre-planned installation location, with Raspberry Pi required
4	1	AI Camera	Pre-planned installation location (voltage: DC3.3 V; power: 0.13 W)
5	4	VL53L1X Time-of-flight sensor	Mainly for four-point support and free steering
6	8	Omni-directional wheel	Mainly for single-axis steering (voltage: DC24V; power: 36 W)
7	6	ASME-04B high torque servo	Control and data transmission center (voltage: DC5V; power < 0.3 W)
8	1	ESP32-WIFI MCU	PWM control forward and reverse rotation and speed (voltage: DC7.4 V; power: 4.2 W)
9	2	EVO-P5Ti-UT continuous rotation servo with 360-degree	For anti-slip applications and improving tire-to-ground engagement
10	2	Rubber tread	Self-designed (single-layer printing thickness 0.6 mm; PLA material)
11	2	3D-printed wheel frame	Supplying 20 sets of electromagnet power requirements (DC24V → DC12.5 V) and equipped with large-area cooling fins
12	1	10A automatic buck-boost power supply module	Servo motor with 360-degree rotation (DC24V → DC7.4 V); ESP32, LED SMD 5050 (DC24V → DC12V)
13	2	LM2596 Buck Module	Single-group four rows parallel output voltage, up to 15A
14	2	Fixed terminal block	Controls electromagnet adhesion switch; switching frequency up to 5 MHz, fast response
15	2	MOSFET relay module	

According to the simulation results shown in Fig. 3, the maximum deformation of the L2 member in the x-axis direction was 1.788 mm, and the deformation of the L3 member was 1.769 mm, which was not significantly different. The maximum deformation in the y-axis direction was observed in the L3 member, which was 0.619 mm. The results indicated that the L3 member experienced the highest force, but the deformation was small and met the design requirements.

The study features a symmetric modular design composed of four modules: M0, M1, M2, and M3, as displayed in Fig. 2(c). M0, which functions as the core module and control center, houses a microcontroller that governs various motors and relays. Meanwhile, M1 and M2 are extension arms that can be elongated to increase the robot's range. On the other hand, M3 is the footpad module equipped with up to 10 electromagnets for adhesion to steel plates. After testing various methods, magnetic adhesion was deemed the most appropriate for the robot's primary target, which is steel structures, as indicated in Table 2. The footpad module is designed to resemble the sole of a human foot, with a four-sided rectangular shape and ultra-thin thickness for reduced weight and fit in narrow spaces. The outermost layer of the footpad module is made of aluminum alloy and measures 225 mm (length) x 110 mm (width). A photo of the footpad module and its 3D design can be seen in Fig. 4.

Magnetic adhesion was the most suitable method for this robot's primary targets, which were steel structures, as shown in Table 2. Fig. 4 presents a photo of the footpad module and a 3D design of its parts. The footpad module is designed to be similar to the sole of a human foot, with a four-sided rectangular shape and ultra-thin thickness to reduce overall weight and fit into narrow rectangular spaces. The outermost layer of the footpad module is made of aluminum alloy and measures 225 mm (length) x 110 mm (width). To not causing the internal electromagnets from deformation due to excessive rotation, compression, or bending moments, the design integrates a 90-degree inward bend around the edges. The second layer from the outside is a custom-printed

bracket created using 3D printing technology and PLA material to position screws and reinforce the electromagnets. The footpad module also incorporates the ToF sensor (VL53L1X) and LED (SMD 5050), which detect the distance between the footpad and the steel plate to avoid footpad collision that can cause damage to the structure and provide illumination in dimly lit environments.

This study implemented a unique design in the M0 core module by adding a pair of continuously rotating servo-driven wheels to the position of member L3. These wheels can facilitate forward and backward movement or turning on the ground, as shown in Table 3. The HMICRobot adopted a hybrid power design, which can switch between modes to meet the requirements of precise torque and movement on steel plates during climbing and the need for fast movement on the ground. Notably, the wheels were not placed at both ends to reduce the complexity of the footpad design and ensure that the robot can still switch to footpad mode for movement if the wheels fail.

The hybrid power design enables the proposed HMICRobot to switch freely between four modes: driving, walking, climbing, and inspection, as shown in Fig. 5. The driving mode uses wheels for fast movement on flat surfaces and can quickly switch to walking mode as needed. The robot can switch to the climbing mode when encountering obstacles or steel diaphragms. In inspection mode, the footpad adheres to a steel plate, and the robot can transform into a mechanical arm to perform inspection tasks using a camera.

2.2. Turning-moment analysis for climbing over the steel diaphragms

HMICRobot attaches a footpad to the steel plate when climbing over steel barriers and rotates 360 degrees to cross the barrier. This action causes bending moments on the footpad, and the magnitude of these bending moments is directly proportional to the distance between the robot's center of mass and the center of the footpad. Fig. 6 (a) shows the footpad's design and the electromagnets' positions. Fig. 6 (b) schematically shows the maximum bending moment $M_{x, \max}$ and $M_{y, \max}$ with respect to the center point O of the footpad, which is symmetric about the x-axis and the y-axis.

Due to the bending moment caused by flipping, it is necessary to consider whether the resisting bending moment produced by the footpad's electromagnetic force can counterbalance the flipping moment of the robot. The resistive bending moment produced by the electromagnetic force at the footpad can be calculated by determining the specifications and positions of the electromagnets. The flipping moment can be modified by adjusting the position of the robot's center of mass through retraction. The distance from the center of mass to the footpad center ($C_{M, \text{distance}}$) is then determined using the robot's weight and the electromagnets' design.

The value of $C_{M, \text{distance}}$ is calculated by first determining the value of $M_{x, \max}$ using Eqs. (1) and (2), which is smaller than that of $M_{y, \max}$. Therefore, $M_{x, \max}$ is used to calculate the $C_{M, \text{distance}}$ value, which is useful for controlling the robot during the flipping process. The magnetic forces produced by the electromagnets n4, n1, and n2 are measured as $F_{N_e, n4}$, $F_{N_e, n1}$, and $F_{N_e, n2}$, respectively. Fig. 7 illustrates the lever arms of these magnetic forces in their respective directions, connected point O, which are represented by d' , d , and R_d . The total mass of the robot is represented by m .

$$M_{x, \max} = 2 \left(F_{N_e, n4}(d') + F_{N_e, n1}(d) + F_{N_e, n2} \left(\frac{1}{2} R_d \right) \right) \quad (1)$$

$$C_{M, \text{distance}} = \frac{M_{x, \max}}{m} \quad (2)$$

The calculated $C_{M, \text{distance}}$ values, using theoretically designed and actual measured value, are listed in Table 4. The $C_{M, \text{distance}}$ value obtained from theoretical value of $M_{x, \max}$ is 33.99 cm, while that obtained from actual measured value of $M_{x, \max}$ is 19.56 cm. The distance is shorter because the actual electromagnetic force is smaller than the

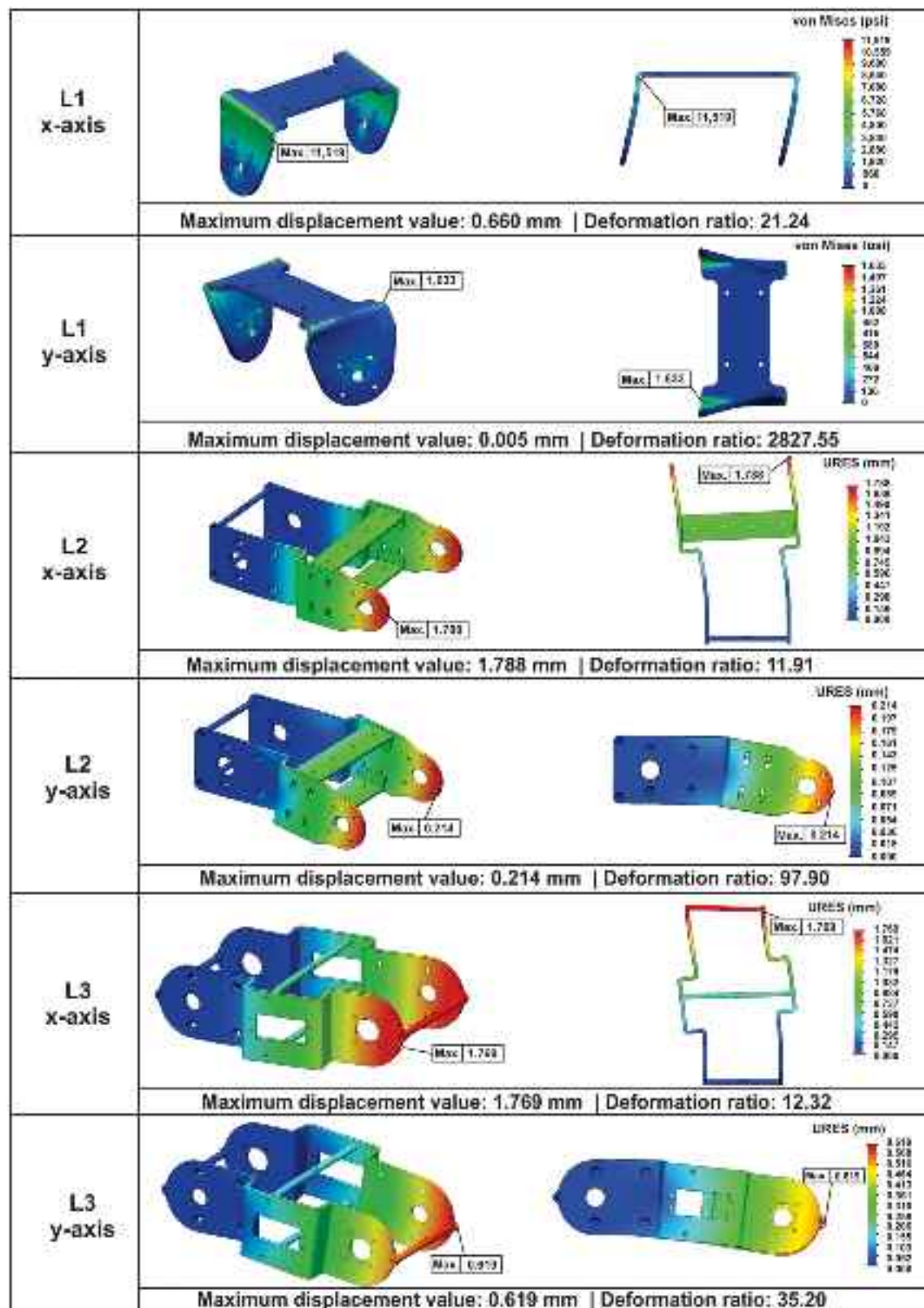


Fig. 3. Displacement analysis of member L1 to L3.

theoretically designed force. The table also indicates that regardless of the theoretical design or actual measurement, $M_{x, \text{max}}$ values are smaller than $M_{y, \text{max}}$.

2.3. Design of integrated mechatronic systems

Fig. 8 shows the mechatronic integration design of HMICRobot, which is controlled by one ESP32-WIFI (NodeMCU-32S) microcontroller. The robot is equipped with six sets of ASME-04B high-torque servos,

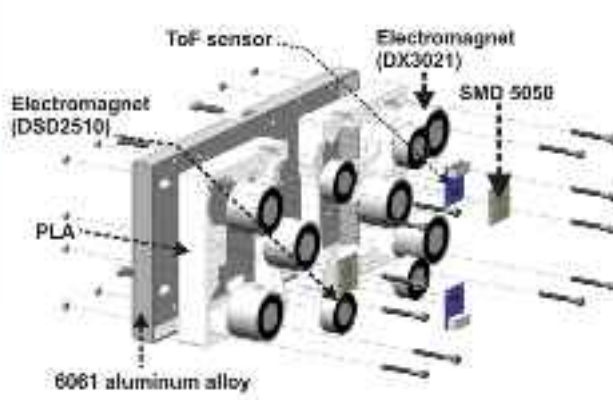
Table 2

Comparison of advantages and disadvantages of adhesion methods.

Type	Attachment mechanism	Advantages	Disadvantages	References
Magnetic	Permanent magnets or electromagnets	Strongest adhesion	Limited to use in magnetically conductive environments	[6,7,9–12,17,18,22–25,27,29,30,36,37]
Negative-pressure	Vacuum suction	Wide applicability	Generally requires smooth walls with no gaps	[8,20,28,34,35,38,39]
Bionic	Van der Waals forces	Highest adaptability	Challenging design due to low adhesion and space constraints	[11,40,41]



(a)



(b)

Fig. 4. HMICRobot footpad module: (a) photo and (b) exploded view.

Table 3

Comparison of advantages and disadvantages of climbing methods.

Type	Advantages	Disadvantages	References
Crawler	High bearing capacity, with the ability to move across undulating terrain	Large volume and weight, limiting movement to one plane	[6,7,22,29,30,32,38–41]
Wheeled	Fast and flexible movement on flat surfaces	High requirement for wall flatness	[8–10,17,18,24,31,33–37]
Legged	Multiple degrees of freedom, allowing for efficient obstacle avoidance	Complex joint control requiring integration of software and hardware	[9,11–13,18,20,23,25,27,28]

relay modules, three voltage reduction modules, 20 electromagnets, two continuous rotation servos, and four sets of time-of-flight sensors. To enhance the interaction between the hardware components, all the parts are symmetrically arranged, and signal wires are located on the upper row while power wires are on the lower row to prevent wire pulling and disconnection issues during the climbing process.

The ASME-04B high-torque servo motor is designed for medium to large-sized robotic arms and has high responsiveness, large stroke, strong anti-interference ability, high stability, and compatibility with various remote control systems. It also integrates stable power technology and fuse protection to reduce the chances of disconnection during climbing. However, the factory-set torque limit of the servo is 380 kgf-cm, while the actual torque value measured in this research is 240 kgf-cm.

The power supply setup is a critical factor for the proper operation of the robotic system, as shown in Fig. 9. The Twintex TP-2305PU power

supply is used to power each unit of the climbing robot to ensure stable power output over extended periods. The power cables are concentrated at the output end of the 24 V power supply, and four output voltage specifications are provided, including DC24 V, DC12.5 V, DC12 V, and DC7.5 V. While the ASME-04B servomotor, with a DC24 V specification, can be powered directly, other components, such as electromagnetic coils and 7.4 V continuous rotation servos, must be powered through a step-down board. To avoid power outages during the climbing process, adequate heat dissipation must be ensured when the step-down board power continuously operates for a prolonged period. Therefore, a metal body and heat-dissipation fins stabilize the electrical control system. Additionally, the step-down power supply method is preferred since boost conversion efficiency is lower than step-down conversion efficiency.

The built-in ESP32 allows for a wireless control interface to facilitate the robot's movement, climbing, and testing. A mobile phone or personal computer (PC) browser can wirelessly connect to the same Wireless Access Point (WAP) location to operate the servo motor on the webpage. The wireless technology uses the WebSocket network transmission protocol, a non-blocking communication method that simultaneously connects multiple devices and has real-time control capability. This avoids the climbing robot restarting due to connection anomalies and immediately returning to the initial state, ensuring the smoothness of operation and compliance with the operation logic.

3. Experimental design

Experiments were conducted to present the capabilities of the HMICRobot. The first experiment, **case 1**, aimed to measure the adhesion force of the robot's footpads. The second experiment, **case 2**, was conducted to show the ability of the HMICRobot to transition from driving to walking mode was verified. Experiments 3–6, **cases 3–6**, demonstrated the HMICRobot's ability to climb over cornered structures, in which an L-shaped thin steel plate was used as a model to simulate the diaphragm in a steel box girder.

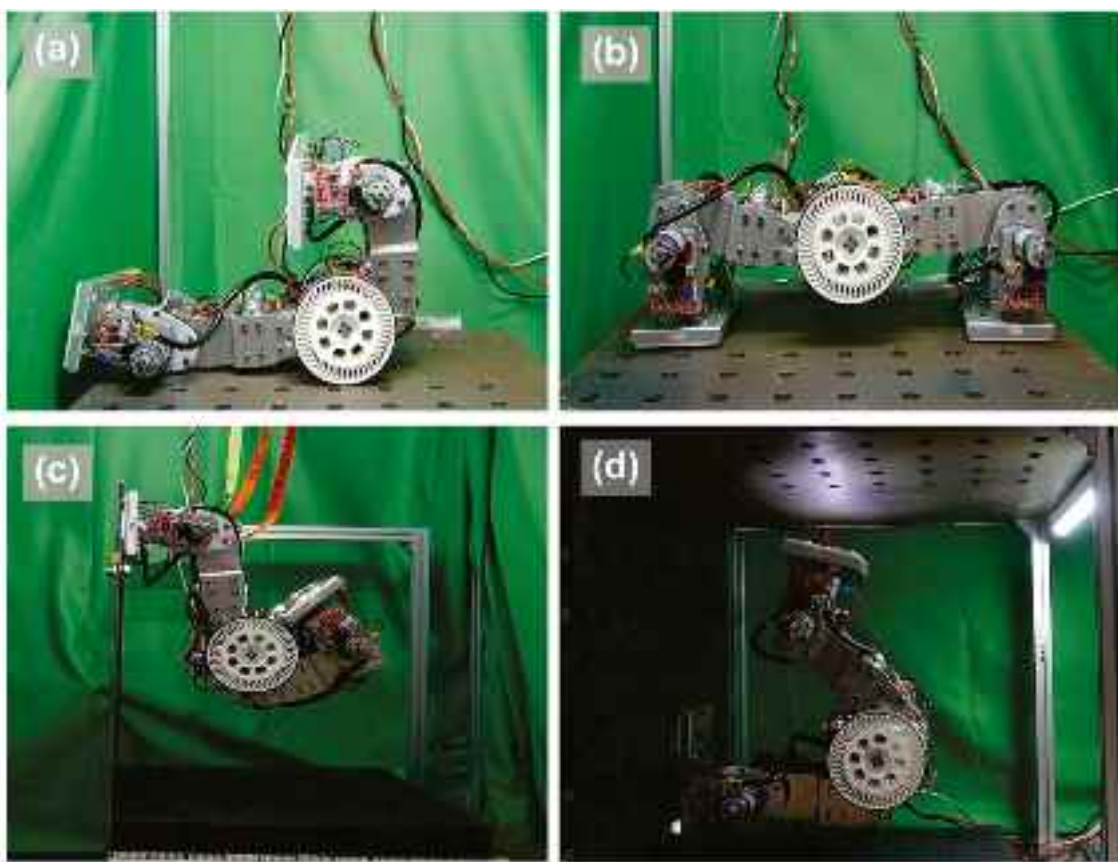


Fig. 5. Four modes of HMICRobot: (a) driving mode, (b) walking mode, (C) climbing mode, and (d) inspecting mode.

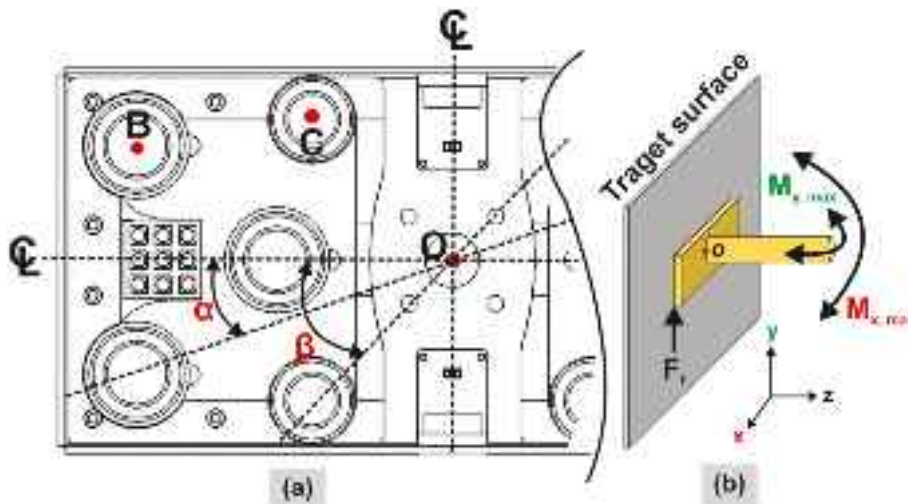


Fig. 6. (a) Axisymmetric view of the center of the footpad; (b) $M_{x,\max}$ and $M_{y,\max}$ and refer to the maximum bending moments in the transverse and longitudinal directions, respectively.

Case 1. Study on Adhesion Force of Footpads.

The actual magnetic adhesion of the footpad played a crucial role in determining whether the HMICRobot could successfully climb and traverse the L-shaped thin steel plate. Therefore, a footpad was removed from the HMICRobot and subjected to a fixed directional load to measure the total electromagnetic force. One footpad was selected, and all the electromagnetic coils were checked to ensure they could be energized and de-energized correctly. Then, a 5-mm-thick steel plate was fixed to a Universal Testing Machine (UTM) base, and the footpad was

placed on top. A hydraulic jack was used to pull the steel plate upward at a 2 mm/min speed until it detached or slid. The adhesion state of the footpad's electromagnetic coils was observed. Fig. 10 displays the actual adhesion force test of the footpad. The left image shows the positive adhesion force test of the footpad, and the right image shows the sliding friction force test of the footpad under an applied load.

Case 2. Study on the Transition from Driving to Walking Mode.

In this experiment, we aimed to demonstrate the HMICRobot's ability to transition between driving and walking modes. We placed the

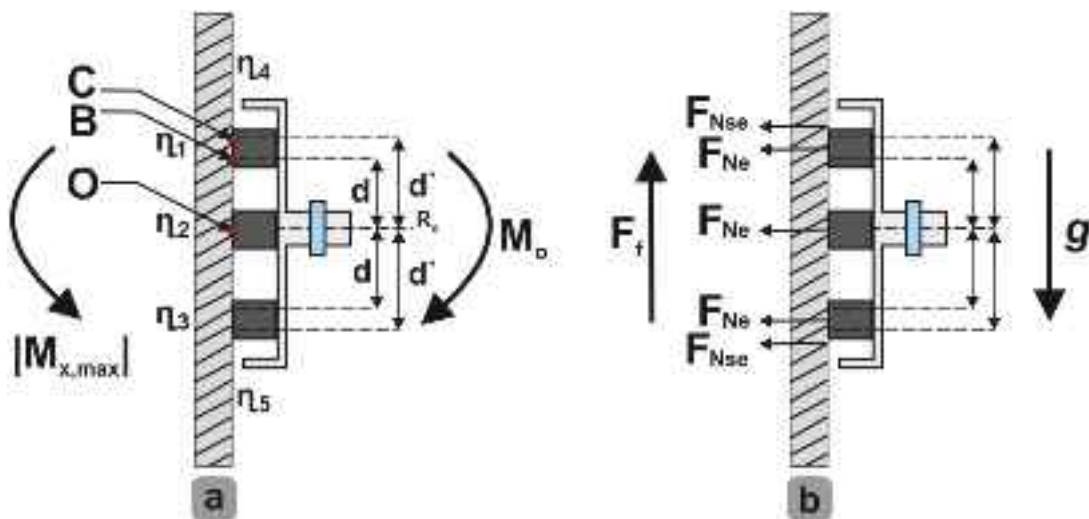


Fig. 7. Diagrams of (a): bending moment and (b): the friction area.

Table 4

Theoretical and measured values for various parameters of the footpad, including maximum bending moment (M), magnetic force (F), and distance from mass center to footpad center (C_M).

Parameter	Theoretical value	Measured value
$ M_x, \max $	338 kgf-cm	194.5 kgf-cm
$ M_y, \max $	716 kgf-cm	397 kgf-cm
$F_{N_e, n4}$	9 kgf	6.5 kgf
$F_{N_e, n1}$	28 kgf	15 kgf
F_{total}	194 kgf (1902.49 N)	110.02 kgf (1078.93 N)
F_f, total	34.92 kgf (342.45 N)	20.93 kgf (205.25 N)
$C_M, \text{distance}$ ($m = 9945 \text{ g}$)	$\approx 33.99 \text{ cm}$	$\approx 19.56 \text{ cm}$

robot on a horizontal surface with a 10-degree inclined steel plate while it was in driving mode, then used the web control interface to switch to walking mode. We recorded the changes in angle and the process of the HMICRobot after the switch for subsequent analysis.

Case 3. Study on the Transition from Driving to Climbing Mode.

This experiment aimed to study the process of the HMICRobot transitioning from driving to climbing mode and climbing up a steel plate wall from the ground level. Initially set to driving mode, the HMICRobot was driven towards the left, stopping at 30 cm from the steel plate wall, as shown in Fig. 11a. The center of gravity was adjusted by sequentially rotating the J5 and J4 joints to shift it to the left of the wheel center, preparing for climbing. Next, the J3 and J2 joints were

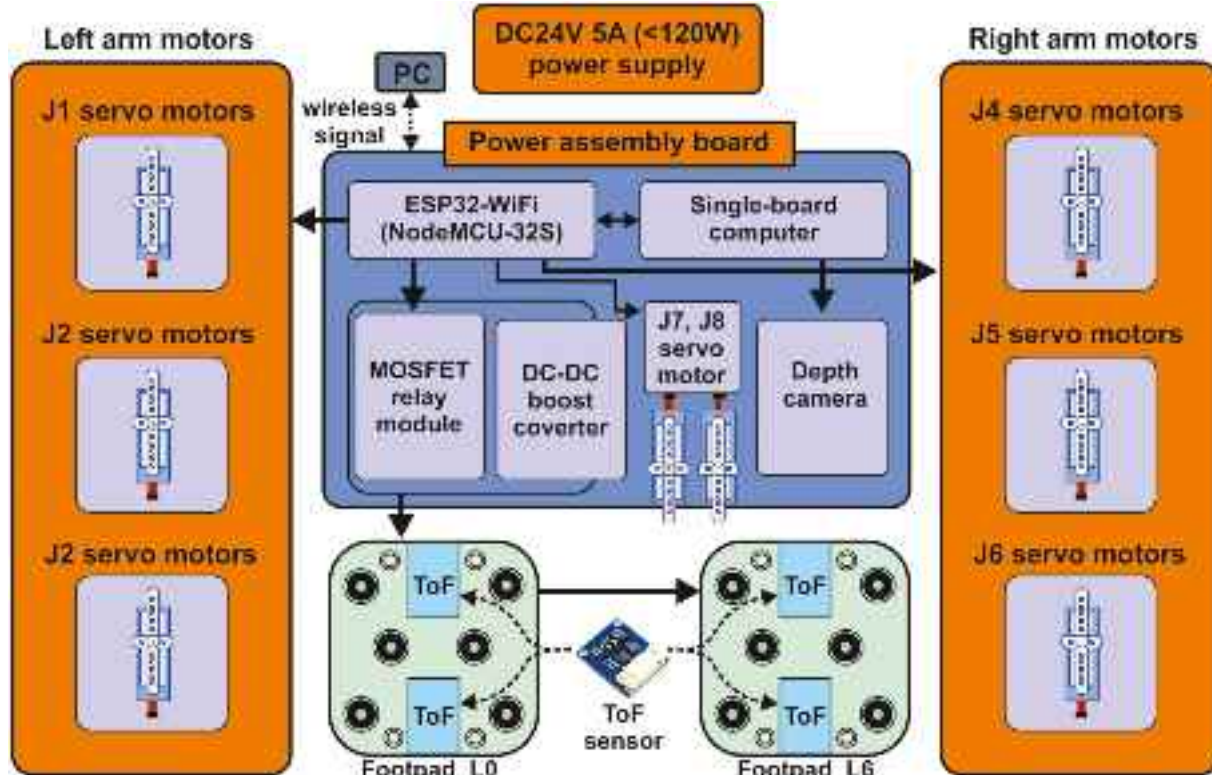


Fig. 8. Hardware design of HMICRobot's mechatronic system.

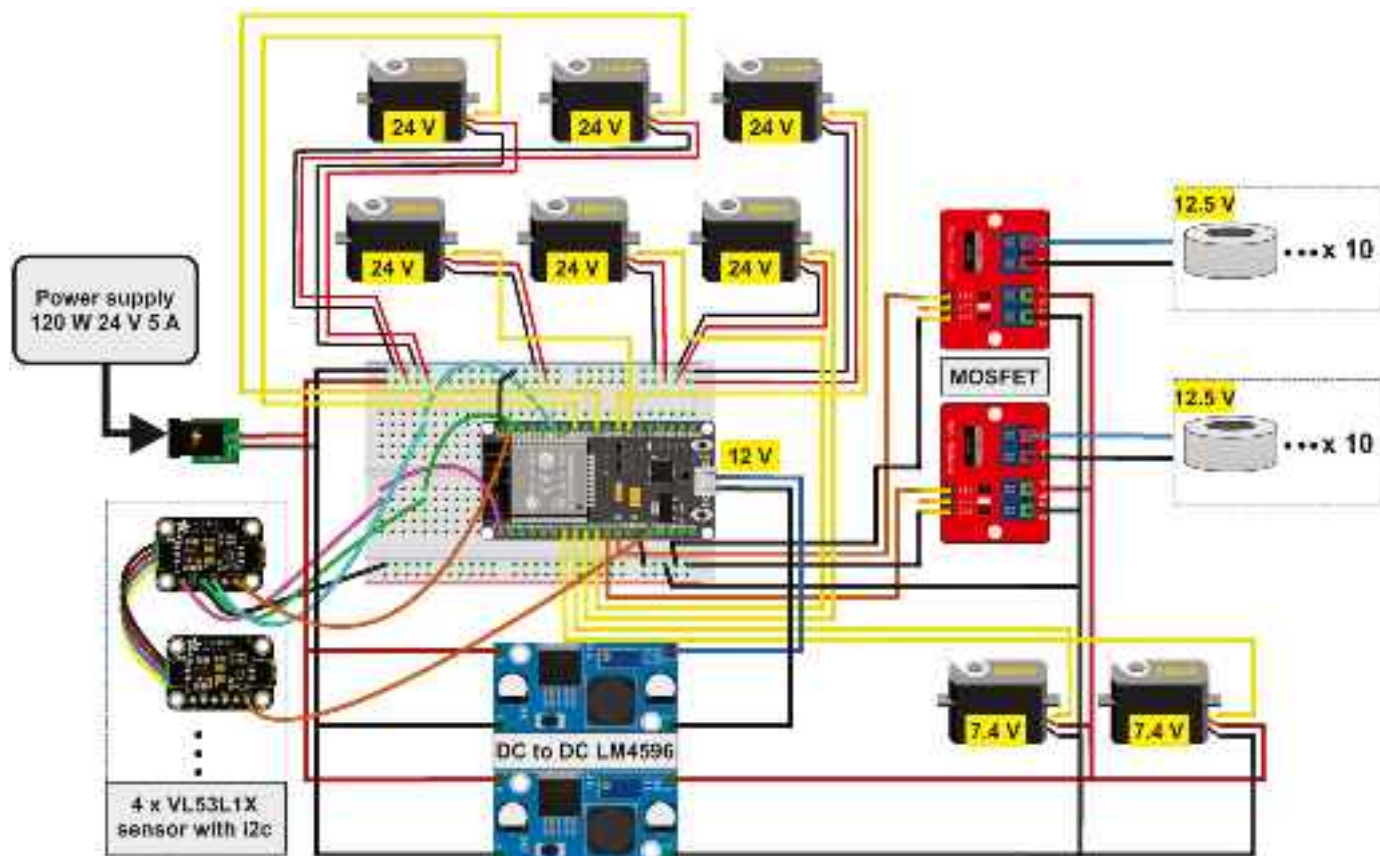


Fig. 9. Power-circuit plan.



Fig. 10. In-situ adhesion force testing of the footpad: (a) the positive adhesion force test and (b) the sliding friction force test for directional loading of the footpad.

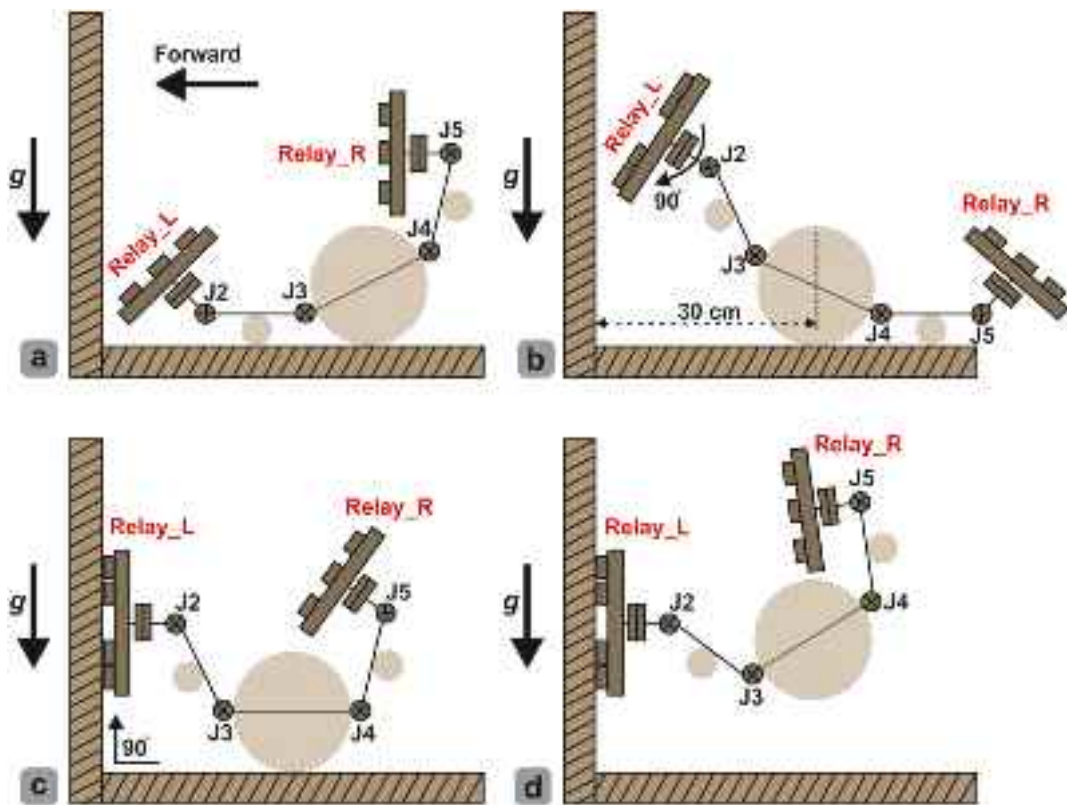


Fig. 11. Illustration of the path for transitioning from driving to climbing mode.

rotated sequentially to raise the left footpad and magnetically attach it to the steel plate wall, as depicted in Fig. 11b and c. Once the left footpad's electromagnet was powered on and securely adhered to the steel plate, the HMICRobot began climbing by sequentially rotating the J5, J4, J3, and J2 joints. During the joint rotations, the HMICRobot's center of mass was kept close to the steel plate wall to minimize the bending moment on the footpad.

Case 4. Investigation of Climbing over on L-Shaped Thin Steel Plates Simulating Diaphragms in Steel Box Girder Bridges.

We used an L-shaped thin steel plate as a demonstration model to verify the HMICRobot's ability to climb over diaphragms in steel box girder bridges. The HMICRobot can directly cross a diaphragm that is

200 mm in height and 5 mm in thickness. However, when the diaphragm height exceeds 200 mm, a flipping motion is required to pass over the thin plate. Fig. 12 illustrates three stages of the simulated flipping process using the L-shaped thin steel plate. First, the right footpad (Relay_R) adheres to the edge of the steel plate, as shown in Fig. 12a. Next, the left footpad (Relay_L) is released, as shown in Fig. 12b. The HMICRobot then makes a 360-degree rotation to cross over the thin steel plate, adhering to the other side with the electromagnet activated. Finally, the right footpad is released, and the HMICRobot turns by 360 degrees again to flip over the thin steel plate and cross to the other side, as shown in Fig. 12c.

Case 5. Investigation of Lateral Right-Angle Climbing.

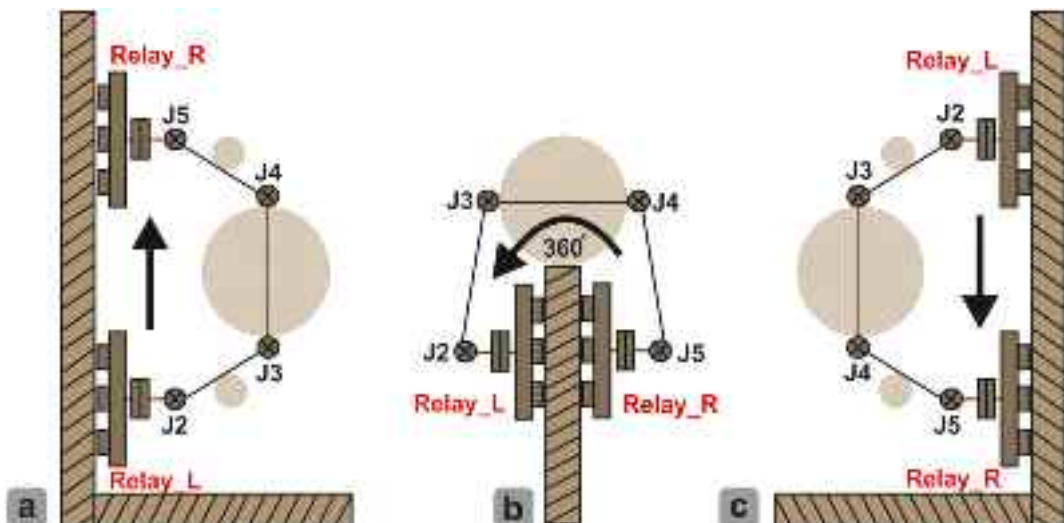


Fig. 12. Illustration of the path for climbing over on L-shaped thin steel plates.

The HMICRobot was implemented for lateral right-angle climbing, and various aspects of the robot's design were investigated. The potential applications of the robot for this type of climbing were explored, including its mechanical design and attachment force. An experimental climbing path, $a \rightarrow b \rightarrow c$, was used to test the robot, and Fig. 13 shows the path with the direction of gravity g pointed into the paper surface. The HMICRobot's mechanical stability and possible slippage between the footpad and the steel plate was closely monitored during the climbing process.

Case 6. Study of Inverted Climbing from Vertical to Horizontal Surfaces.

This experiment focuses on implementing the HMICRobot for inverted, suspended climbing and investigating its mechanical design, adhesion forces, and real-world climbing applications. The HMICRobot climbed along the path $a \rightarrow b \rightarrow c$, as shown in Fig. 14, transitioning from a vertical steel plate to a suspended horizontal plane. The direction of gravity, g , was downward during the inverted climbing, which helped to reduce slippage. To reduce torque during flipping, the center of mass was positioned as close as possible to the right footpad (Relay_R). The motor for each joint was controlled sequentially in path $J5 \rightarrow J4 \rightarrow J3 \rightarrow J2$, to facilitate the inverted and suspended climb.

4. Results and discussion

4.1. Experimental results

4.1.1. Results of studying the adhesion force of footpads

The results of the electromagnetic adhesion force experiment are presented in Fig. 15, showing the actual positive adhesion force (black) and the lateral friction force (red) over time. The actual positive adhesion force steadily increased from 0 to 366 s before suddenly dropping after reaching a maximum value of 110.02 kgf due to the partial detachment of the electromagnets from the steel plate. Although some electromagnets detached, the remaining ones could provide adhesion force and increase the force after the drop, though not to the previous maximum level. We took the highest peak before the adhesion force was reversed to determine the maximum adhesion force value. The lateral friction force increased until 20.93 kgf, where it started to slip.

Fig. 15 shows that the footpad undergoes processes such as reattachment to the electromagnet and slipping during the application of force. To be conservative, we take the maximum lateral friction force of the footpad as 20.93 kgf, which was the value before slippage occurred. The experimental results also indicate that the lateral adhesion force is smaller than the positive adhesion force, suggesting that vertical climbing and flipping are more challenging than horizontal inverted climbing.

4.1.2. Results of studying on transforming process from driving to walking mode

The experimental results demonstrate that the HMICRobot can successfully transition from driving to walking mode, as shown in Figs. 16 and 17. The robot's rubber tires, omni-directional wheels, and dual footpads provided sufficient resistance to prevent slipping when operating on a horizontal surface or a subtle inclined surface, as depicted in Fig. 16. However, on steeper slopes, like the 10-degree inclined surface shown in Fig. 17, the right footpad must be magnetically attached to the steel plate for stability before lifting the left swing arm. This step prevents the HMICRobot from sliding to the left due to low friction. It is important to note that the steel plate and electromagnets provide little friction when there is no adhesion force. Thus, the HMICRobot can smoothly switch modes without requiring the magnetic adhesion function of the electromagnets when transitioning on flat or subtly inclined surfaces.

4.1.3. Results of studying on climbing over L-shaped thin steel plates

The climbing sequence shown in Fig. 18 demonstrates that the HMICRobot can climb over an L-shaped thin steel plate, but this task is challenging and requires special precautions. During the experiment, the machine tended to fall due to excessive torque when transitioning from horizontal to vertical when switching from driving to climbing mode. To address this issue, it is recommended to rotate the footpads' direction so that the vertical footpad can adhere to the steel plate. This increases the resistance of the footpad's electromagnets to bending moments, improving the machine's stability during the transition. Additionally, an offset center of gravity caused excessive deviation, making climbing more complex and less stable. Moreover, when the HMICRobot was curled in the opposite direction, the internal power cable's reserved length was insufficient, resulting in the power supply interface of the servo motor becoming disconnected. This caused the cable to become excessively stretched, leading to the loss of control and a fall.

4.1.4. Results of studying lateral right-angle climbing and inverted climbing from vertical to horizontal surfaces

Figs. 19 and 20 present the experimental results showcasing the climbing capabilities of the HMICRobot. In the lateral right-angle climbing experiment shown in Fig. 19, the robot demonstrated stable switching between two steel plates with a horizontal deviation of the moving footpad of <10 mm relative to the fixed-end footpad. Unlike the HyReCRo robot proposed in the literature [42], the HMICRobot developed in this study does not require additional friction materials and is slip-resistant, making it less likely to fall. The inverted climbing experiment, shown in Fig. 20, demonstrated the HMICRobot's successful performance in inverted climbing, a rare feat among inchworm robots. According to the experiment, the ideal distance between the two footpads during inverted climbing is approximately three footpad widths or

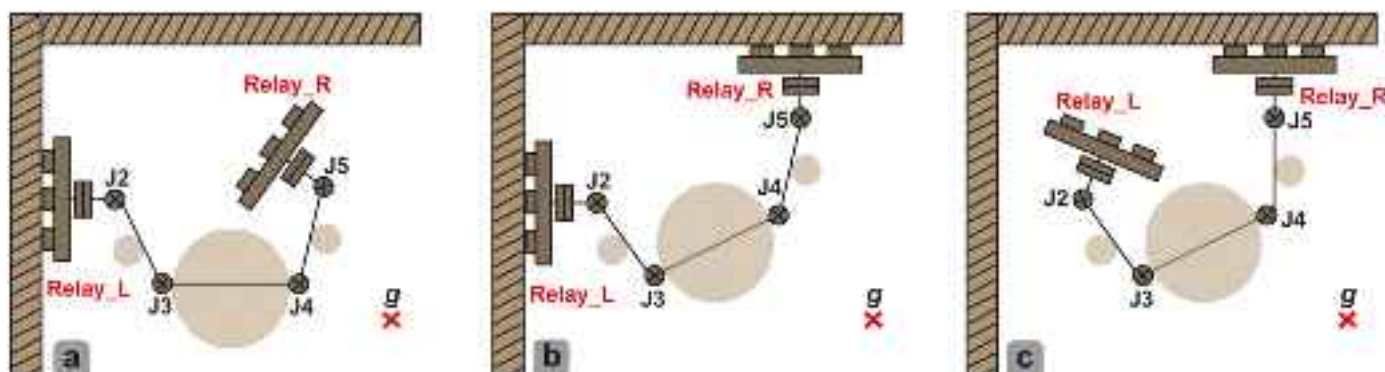


Fig. 13. Illustration of the path for Lateral Right-Angle climbing.

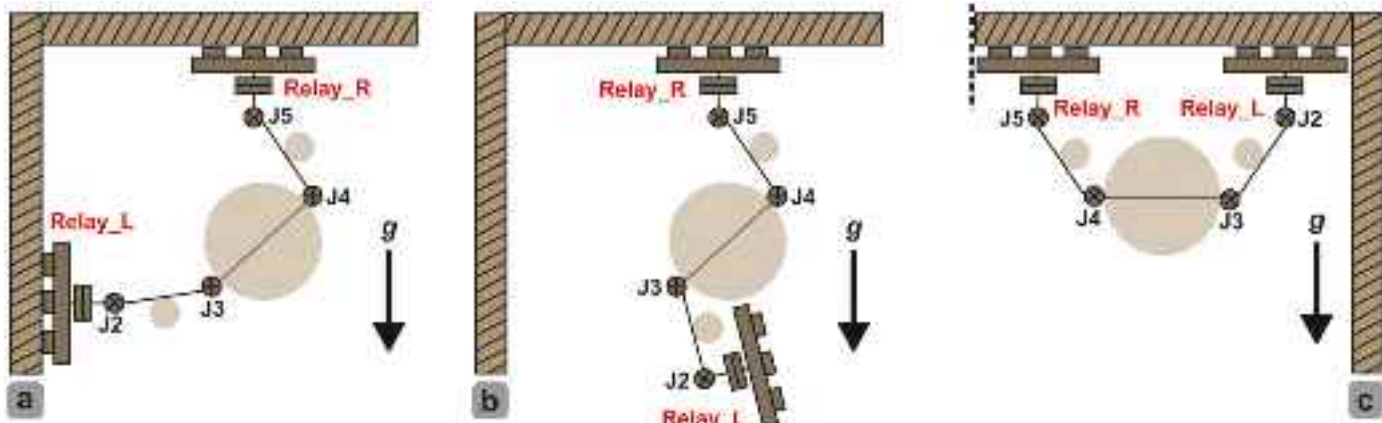


Fig. 14. Illustration of the path for inverted climbing from vertical to horizontal surfaces.

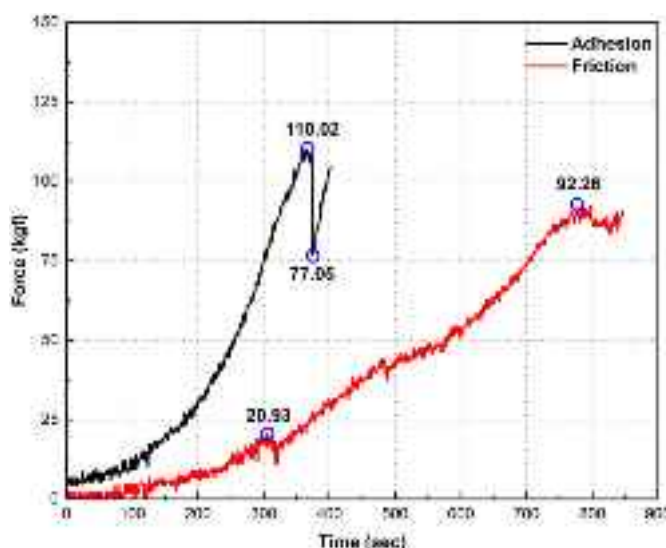


Fig. 15. Time-dependent measurement of the positive electromagnetic adhesion force (black) and lateral friction force (red) of the HMICRobot's footpads. (For interpretation of the references to colour in this figure legend, the reader is referred to the web version of this article.)

330 mm. The experiment also showed that the HMICRobot, with its center of gravity close to the left steel plate, was slowly able to lift the right arm until the right footpad gradually became parallel to the upper steel plate before being powered to adhere to the horizontal steel plate. The left footpad was then detached from the steel plate, and the left arm was flipped until the left footpad gradually adhered and conformed to

the upper steel plate. Overall, this experiment proved that the HMICRobot, based on its design, can perform actual inverted climbing.

4.2. Discussion

In terms of climbing and obstacle avoidance abilities, tracked robots [6,7,22,26,29,30,32,38–41] and wheeled robots [8–10,17,18,24,31,33–37] primarily use designs that combine wheels with permanent magnets to ensure stable operation on structure surfaces. However, the literature does not show robots that can overcome higher obstacles or vertical steel diaphragms. Other similar robots [9,11–13,18,20,23,25,27,28,38,39,41,43–45] can climb on magnetic or non-magnetic surfaces, including steel structure surfaces and pipes, and can overcome smaller obstacles. However, they cannot overcome vertical steel diaphragms as targeted in this study. Compared to other robots in the literature, the HMICRobot has been proven in experiments to climb over vertical steel diaphragms.

The design of the HMICRobot features mobility as a key characteristic and incorporates a pair of power wheels on the central core module for ground movement. These two sets of large roller wheels allow forward, backward, and rotational movement, providing greater mobility than existing literature. While other literature [9] features a similar magnetic wheel design to improve mobility on steel structures, they cannot overcome higher obstacles, and the robot becomes immobile if the wheel fails. In contrast, the HMICRobot's design strategy avoids placing wheels at both ends, reducing complexity and ensuring the robot can move to walking mode. The HMICRobot's hybrid power design achieves optimal mobility performance, meeting the precision and torque requirements of climbing steel plates and the speed requirements of moving on the ground by switching modes. With these features, the HMICRobot can operate with stability and adapt to different surfaces

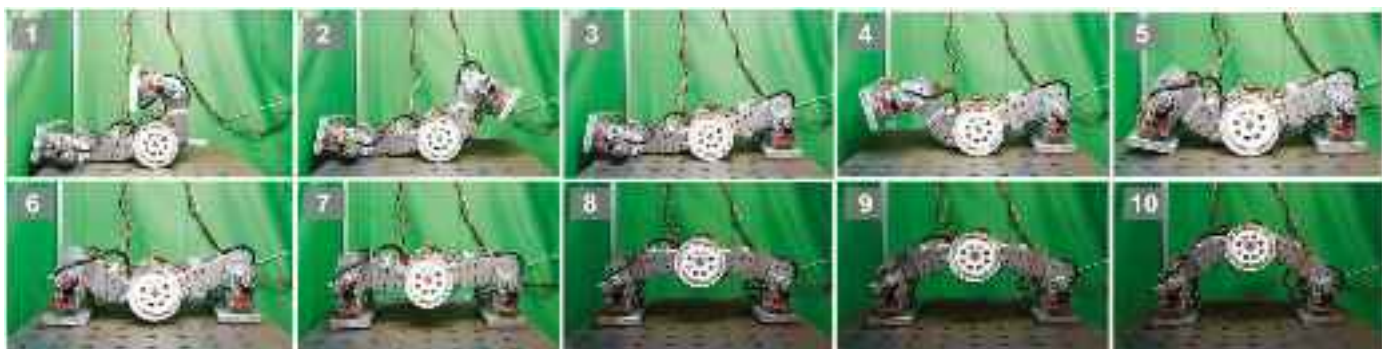


Fig. 16. Mode transformation images of the HMICRobot on a horizontal surface.

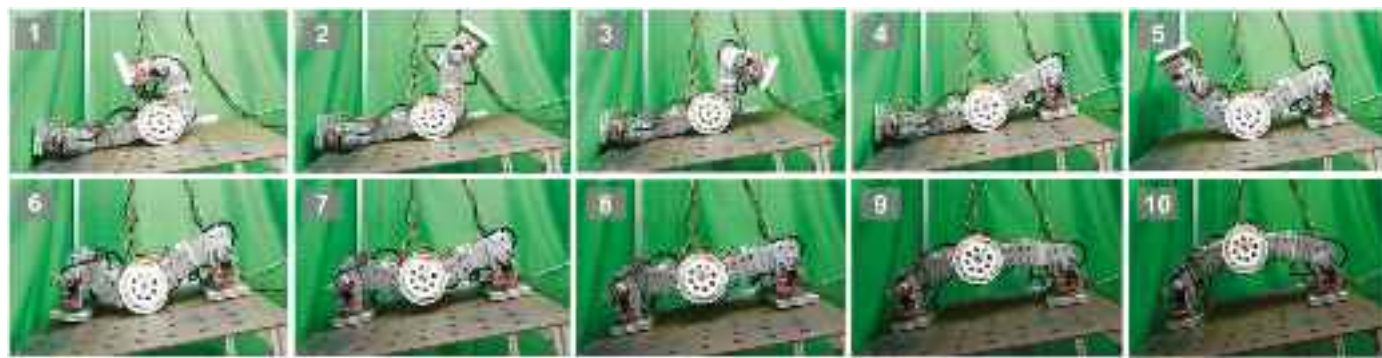


Fig. 17. Mode transformation images of the HMICRobot on a 10-degree inclined surface.



Fig. 18. Sequential images for the HMICRobot climbing over an L-shaped thin steel plate.

and environments.

The HMICRobot exhibits superior locomotion ability compared to similar robots. Its high adhesive force, high-torque servo motor, large angle of rotation, and ability to climb vertically, horizontally, and even upside down enable the robot to perform 360-degree flip obstacle traversal. This character is not achievable by other robots. The robot's high flipping torque capability, precise joint design and control, and accurate control of the footpad electromagnets demonstrate its exceptional performance. To our knowledge, no robots in the literature can perform such actions on vertical steel diaphragms.

Overall, the HMICRobot's design achieves exceptional mobility performance with minimal complexity. Its hybrid power design and

strategy of not placing wheels at both ends enable it to operate with stability and adapt to different surfaces and environments. The unique footpad electromagnetic control and central core module with large-size wheels provide stable and efficient mobility on steel surfaces and on the ground. With the ability to climb vertically and horizontally and perform 360-degree flipping and obstacle-crossing, the HMICRobot is a promising solution for complex inspections and maintenance tasks in steel box girders.

5. Conclusions and future work

This study introduces the HMICRobot, an innovative climbing robot

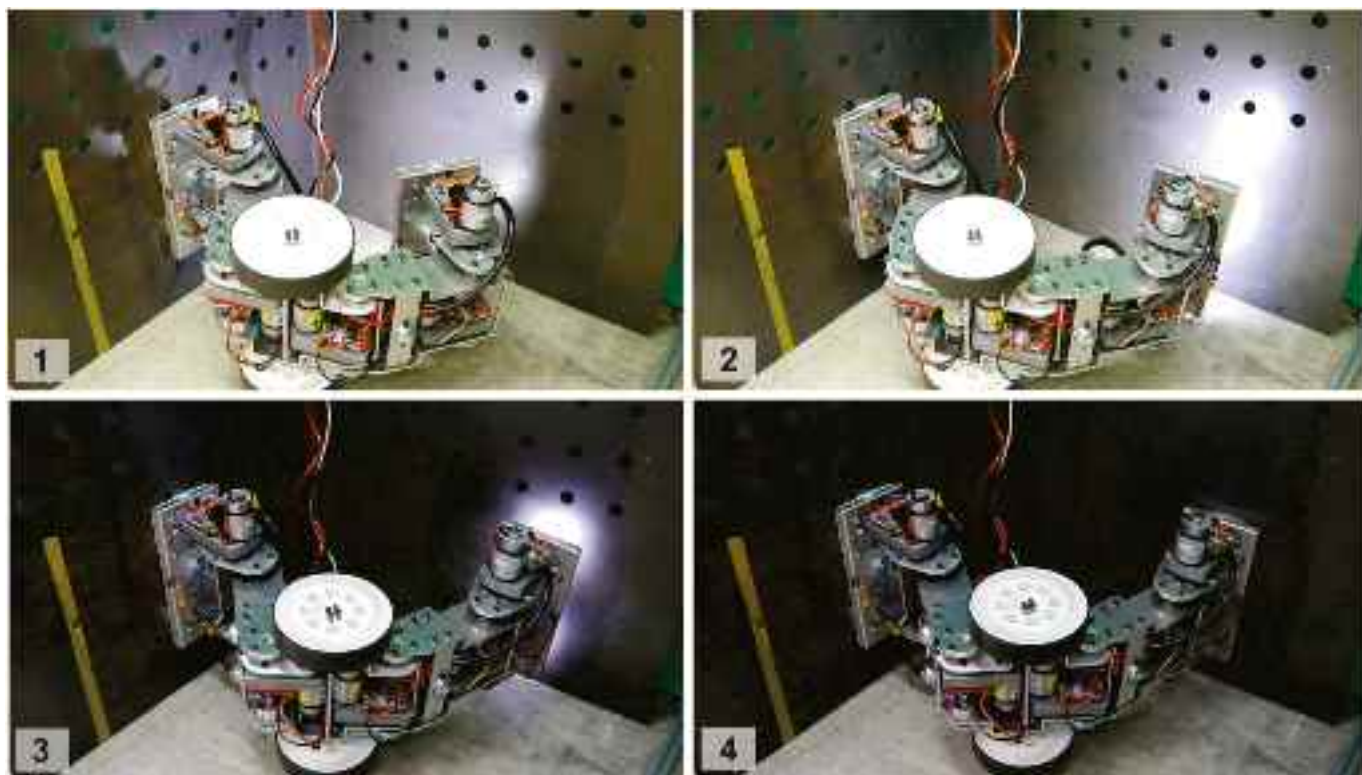


Fig. 19. Images of HMICRobot climbing a lateral right-angle structure.

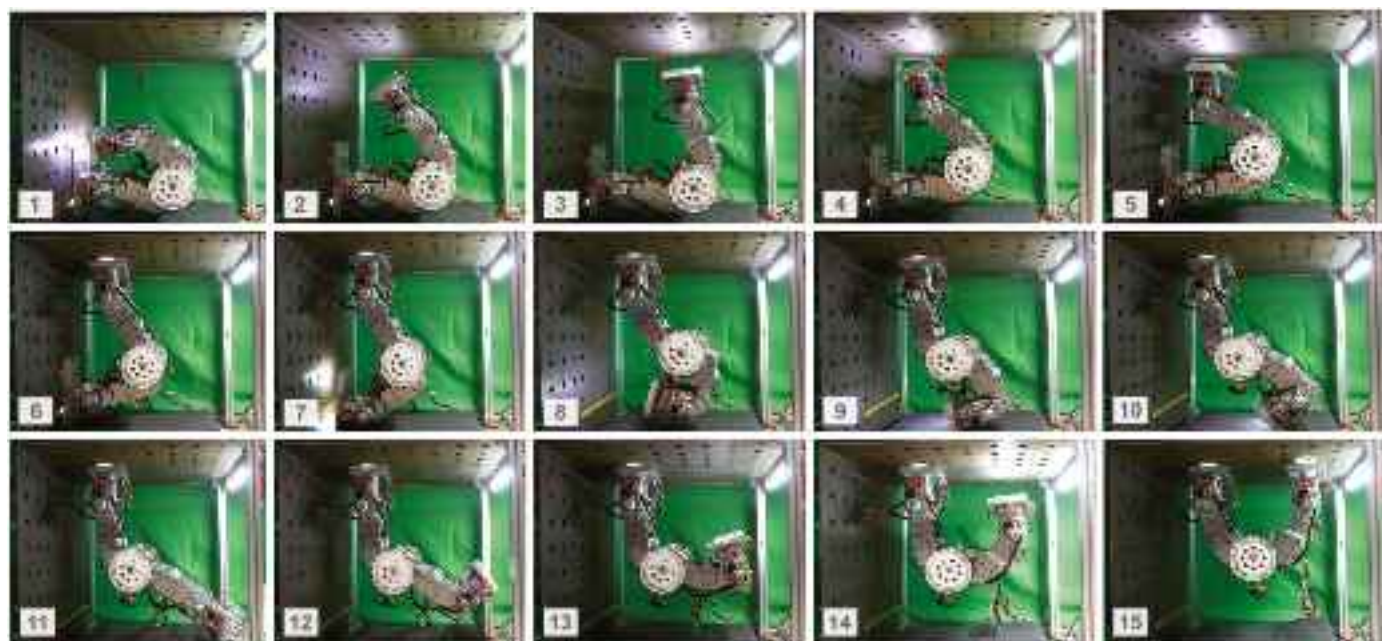


Fig. 20. Sequential images for the HMICRobot's inverted climbing from vertical to horizontal surfaces.

that traverses diaphragms that separate various bridge sections. Building on the design of various magnetic climbing robots, the HMICRobot incorporates their best features and enhances their limitations. The robot can change between four different modes, as demonstrated in experimental results where it was able to traverse L-shaped thin steel plates simulating inspection channels on a steel bridge and perform lateral right-angle climbing and inverted hanging climbing. The HMICRobot's hybrid power design provides both precise torque and

movement required for climbing on steel plates and the necessary speed for ground movement by allowing the robot to switch between modes. The omission of wheels at both ends simplifies the design of the footpads and ensures that the robot can continue to move in walking mode when the wheels fail. These innovations distinguish the HMICRobot from other existing literature.

Given the advantages of the HMICRobot, several suggested improvements can be made in future work. Firstly, using lightweight

carbon fiber composite materials to replace aluminum alloy and reducing the size and weight of the large torque servos could improve the robot's climbing success rate. Secondly, a PCB board that integrates instrument equipment to optimize power management and reduce the risk of short circuits would allow the robot to use lithium batteries. Thirdly, a flexible mechanism design could improve the adhesion force on uneven surfaces. Fourthly, the robot's stability in the presence of vibrations should be evaluated. Fifthly, future work can explore AI-based control to enhance movement speed and enable self-judgment of the best adhesion position. Lastly, a comparison with similar robots can reinforce the contributions and advancements of the HMICRobot.

Future testing and in-field experiments are necessary to evaluate the robot's potential use in real-world applications. It includes testing under various environmental conditions, evaluating endurance and reliability, testing load capacity and stability under various possible conditions, and conducting in-field experiments in bridge inspections or maintenance to provide valuable insights into the robot's performance and potential benefits.

Supplementary data to this article can be found online at <https://doi.org/10.1016/j.autcon.2023.104905>.

Declaration of Competing Interest

The authors declare that they have no known competing financial interests or personal relationships that could have appeared to influence the work reported in this paper.

Data availability

Data will be made available on request.

Acknowledgments

The authors would like to thank the National Science and Technology Council, Taiwan, R.O.C, for financial support of this research (IDs: MOST 107-2218-E-008-016-MY2; MOST 109-2221-E-008-003-MY3).

References

- [1] S. Phillips, S. Narasimhan, Automating data collection for robotic bridge inspections, *J. Bridg. Eng.* 24 (2019) 1–13, [https://doi.org/10.1061/\(ASCE\)BE.1943-5592.0001442](https://doi.org/10.1061/(ASCE)BE.1943-5592.0001442).
- [2] H.M. La, N. Gucunski, K. Dana, S.H. Kee, Development of an autonomous bridge deck inspection robotic system, *J. Field Robot.* 34 (2017) 1489–1504, <https://doi.org/10.1002/rob.21725>.
- [3] T. Le, S. Gibb, N. Pham, H.M. La, L. Falk, T. Berendsen, Autonomous robotic system using non-destructive evaluation methods for bridge deck inspection, in: IEEE International Conference on Robotics and Automation (ICRA), 2017, pp. 3672–3677, <https://doi.org/10.1109/ICRA.2017.7989421>.
- [4] H. Peel, S. Luo, A.G. Cohn, R. Fuentes, An improved robot for bridge inspection, in: Proceedings of the 34th ISARC. 34th International Symposium in Automation and Robotics in Construction, 2017, pp. 663–670, <https://doi.org/10.22260/isarc2017/0092>.
- [5] R.S. Lim, H.M. La, W. Sheng, A robotic crack inspection and mapping system for bridge deck maintenance, *IEEE Trans. Autom. Sci. Eng.* 11 (2014) 419–428, <https://doi.org/10.1109/TASE.2013.2294687>.
- [6] S.T. Nguyen, H.M. La, Development of a steel bridge climbing robot, in: IEEE/RSJ International Conference on Intelligent Robots and Systems (IROS), 2019, pp. 1912–1917, <https://doi.org/10.1109/IROS40897.2019.8967748>.
- [7] X. Gao, L. Yan, G. Wang, L.M. Chen, Modeling and analysis of magnetic adhesion module for wall-climbing robot, *IEEE Trans. Instrum. Meas.* 72 (2022) 1–9, <https://doi.org/10.1109/TIM.2022.3224522>.
- [8] L. Yang, B. Li, G. Yang, Y. Chang, Z. Liu, B. Jiang, J. Xiaol, Deep neural network based visual inspection with 3D metric measurement of concrete defects using wall-climbing robot, in: IEEE/RSJ International Conference on Intelligent Robots and Systems (IROS), 2019, pp. 2849–2854, <https://doi.org/10.1109/IROS40897.2019.8968195>.
- [9] S.T. Nguyen, A.Q. Pham, C. Motley, H.M. La, A practical climbing robot for steel bridge inspection, in: IEEE International Conference on Robotics and Automation (ICRA), 2020, pp. 9322–9328, <https://doi.org/10.1109/ICRA40945.2020.9196892>.
- [10] N.H. Pham, H.M. La, Q.P. Ha, S.N. Dang, A.H. Vo, Q.H. Dinh, Visual and 3D mapping for steel bridge inspection using a climbing robot, in: 33rd International Symposium on Automation and Robotics in Construction (ISARC), 2016, pp. 141–149, <https://doi.org/10.22260/isarc2016/0018>.
- [11] Q. Jiang, F. Xu, Grasping claws of bionic climbing robot for rough wall surface: modeling and analysis, *Appl. Sci.* 8 (2017) 1–15, <https://doi.org/10.3390/app8010014>.
- [12] D. Pagano, D. Liu, An approach for real-time motion planning of an inchworm robot in complex steel bridge environments, *Robotica* 35 (2017) 1280–1309, <https://doi.org/10.1017/S0263574716000047>.
- [13] R.S. Bisht, P.M. Pathak, S.K. Panigrahi, Modelling, simulation and experimental validation of wheel and arm locomotion based wall-climbing robot, *Robotica* 41 (2022) 433–469, <https://doi.org/10.1017/S026357472200025X>.
- [14] W. Siyuan, Research status and future development of wall-climbing robot, in: International Conference on Electronics, Circuits and Information Engineering (ECIE), 2021, pp. 122–130, <https://doi.org/10.1109/ECIE52353.2021.00033>.
- [15] Y. Tian, C. Chen, K. Sagoe-Crentsil, J. Zhang, W. Duan, Intelligent robotic systems for structural health monitoring: applications and future trends, *Autom. Constr.* 139 (2022), 104273, <https://doi.org/10.1016/j.autcon.2022.104273>.
- [16] X. Lu, S. Zhao, X. Liu, Y. Wang, Design and analysis of a climbing robot for pylon maintenance, *Ind. Robot.* 45 (2018) 206–219, <https://doi.org/10.1108/IR-08-2017-0143>.
- [17] A. Sirken, G. Knizhnik, J. McWilliams, S. Bergbreiter, Bridge risk investigation diagnostic grouped exploratory (BRIDGE) bot, in: IEEE/RSJ International Conference on Intelligent Robots and Systems (IROS), 2017, pp. 6526–6532, <https://doi.org/10.1109/IROS.2017.8206562>.
- [18] S.T. Nguyen, H. Nguyen, S.T. Bui, V.A. Ho, H.M. La, Multi-Directional Bicycle Robot for Steel Structure Inspection, Cornell University, 2021. <http://arxiv.org/abs/2103.11522>.
- [19] T. Bandyopadhyay, R. Steindl, F. Talbot, N. Kottege, R. Dungavell, B. Wood, J. Barker, K. Hoehn, A. Elfes, Magneto: a versatile multi-limbed inspection robot, in: IEEE/RSJ International Conference on Intelligent Robots and Systems (IROS), 2018, pp. 2253–2260, <https://doi.org/10.1109/IROS.2018.8593891>.
- [20] M. Minor, H. Dulimarta, G. Danghi, R. Mukherjee, R.L. Tummala, D. Aslam, Design, implementation, and evaluation of an under-actuated miniature biped climbing robot, in: IEEE/RSJ International Conference on Intelligent Robots and Systems (IROS), 2000, pp. 1999–2005, <https://doi.org/10.1109/IROS.2000.895264>.
- [21] S.P. Krosuri, M.A. Minor, Design, modeling, control, and evaluation of a hybrid hip joint miniature climbing robot, *Int. J. Robot. Res.* 24 (2005) 1033–1053, <https://doi.org/10.1177/0278364905057854>.
- [22] J.C. Grieco, M. Prieto, M. Armada, P.G. De Santos, A six-legged climbing robot for high payloads, in: Proceedings of the 1998 IEEE International Conference on Control Applications, 1998, pp. 446–450, <https://doi.org/10.1109/cca.1998.728488>.
- [23] C. Viegas, M. Tavakoli, A single DOF arm for transition of climbing robots between perpendicular planes, in: IEEE/RSJ International Conference on Intelligent Robots and Systems, 2014, pp. 2867–2872, <https://doi.org/10.1109/IROS.2014.6942956>.
- [24] M. Tavakoli, C. Viegas, L. Marques, J.N. Pires, A.T. De Almeida, Magnetic omnidirectional wheels for climbing robots, in: IEEE/RSJ International Conference on Intelligent Robots and Systems, 2013, pp. 266–271, <https://doi.org/10.1109/IROS.2013.6696363>.
- [25] M.B. Khan, T. Chuthong, C.A.O.D. Do, M. Thor, P. Billeschou, J.C. Larsen, P. Manoonpong, iCrawl: an inchworm-inspired crawling robot, *IEEE Access* 8 (2020) 200655–200668, <https://doi.org/10.1109/ACCESS.2020.3035871>.
- [26] S.T. Nguyen, H.M. La, A climbing robot for steel bridge inspection, *J. Intell. Robot. Syst.* 102 (2021) 9322–9328, <https://doi.org/10.1007/s10846-020-01266-1>.
- [27] H.D. Bui, S. Nguyen, U.H. Billah, C. Le, A. Tavakkoli, H.M. La, Control framework for a hybrid-steel bridge inspection robot, in: IEEE/RSJ International Conference on Intelligent Robots and Systems (IROS), 2020, pp. 2585–2591, <https://doi.org/10.1109/IROS45743.2020.9340637>.
- [28] M.J.D. Malley, Army Ant Inspired Adaptive Self-Assembly with Soft Climbing Robots, Harvard University, 2020. <https://ssr.seas.harvard.edu/publications/army-ant-inspired-adaptive-self-assembly-soft-climbing-robots> (Accessed date: 27 February 2023).
- [29] W. Zhang, W. Zhang, Z. Sun, A reconfigurable soft wall-climbing robot actuated by electromagnet, *Int. J. Adv. Robot. Syst.* 18 (2021) 1–10, <https://doi.org/10.1177/1729881421992285>.
- [30] S.T. Nguyen, H.M. La, Roller chain-like robot for steel bridge inspection, in: Proceedings of the 9th International Conference on Structural Health Monitoring of Intelligent Infrastructure, 2019, pp. 890–895. https://scholarsmine.mst.edu/inspire-meetings/2019_meeting/robotic_platform/3/ (Accessed date: 20 April 2023).
- [31] F. Xu, S. Dai, Q. Jiang, X. Wang, Developing a climbing robot for repairing cables of cable-stayed bridges, *Autom. Constr.* 129 (2021), 103807, <https://doi.org/10.1016/j.autcon.2021.103807>.
- [32] Z. Zheng, N. Ding, Design and implementation of CCRobot-II: A palm-based cable climbing robot for cable-stayed bridge inspection, in: International Conference on Robotics and Automation (ICRA), 2019, pp. 9747–9753, <https://doi.org/10.1109/ICRA.2019.8793562>.
- [33] F. Xu, Q. Jiang, F. Lv, M. Wu, L. Zhang, The dynamic coupling analysis for all-wheel-drive climbing robot based on safety recovery mechanism model, *Appl. Sci.* 8 (2018) 1–17, <https://doi.org/10.3390/app8112123>.
- [34] W. Myeong, S. Jung, B. Yu, T. Chris, Development of wall-climbing unmanned aerial vehicle system for micro-inspection of bridges, proceedings of the workshop on the future of aerial robotics: challenges and opportunities, in: International Conference on Robotics and Automation (ICRA), 2019, pp. 20–24. https://ieeearialrobotics-uavs.org/wpcontent/uploads/2019/06/ICRA2019_AerialRoboticsWorkshop_paper_Myeong.pdf (Accessed date: 27 February 2023).

- [35] P. Liang, X. Gao, Q. Zhang, R. Gao, M. Li, Y. Xu, W. Zhu, Design and stability analysis of a wall-climbing robot using propulsive force of propeller, *Symmetry* 13 (2021) 1–12, <https://doi.org/10.3390/sym13010037>.
- [36] J.C. Romão, M. Tavakoli, C. Viegas, P. Neto, A.T. De Almeida, InchwormClimber: A light-weight biped climbing robot with a switchable magnet adhesion unit, in: IEEE/RSJ International Conference on Intelligent Robots and Systems (IROS), 2015, pp. 3320–3325, <https://doi.org/10.1109/IROS.2015.7353839>.
- [37] H. Eto, H.H. Asada, Development of a wheeled wall-climbing robot with a shape-adaptive magnetic adhesion mechanism, in: IEEE International Conference on Robotics and Automation (ICRA), 2020, pp. 9329–9335, <https://doi.org/10.1109/ICRA40945.2020.9196919>.
- [38] W. Wang, K. Wang, H. Zhang, Crawling gait realization of the mini-modular climbing caterpillar robot, *Prog. Nat. Sci.* 19 (2009) 1821–1829, <https://doi.org/10.1016/j.pnsc.2009.07.009>.
- [39] Y.Y. Yuan, W.C. Lu, C.J. Kao, J.J. Hung, P.C. Lin, Design and implementation of an inchworm robot, in: International Conference on Advanced Robotics and Intelligent Systems (ARIS), 2016, <https://doi.org/10.1109/ARIS.2016.7886615>, pp. 1–1.
- [40] R. Chen, A gecko-inspired electroadhesive wall-climbing robot, *IEEE Potent.* 34 (2015) 15–19. <https://ieeexplore.ieee.org/abstract/document/7054047>.
- [41] I.H. Han, H. Yi, C.W. Song, H.E. Jeong, S.Y. Lee, A miniaturized wall-climbing segment robot inspired by caterpillar locomotion, *Bioinspiration Biomimet.* 12 (2017), 046003, <https://doi.org/10.1088/1748-3190/aa728c>.
- [42] A. Peidró, M. Tavakoli, J.M. Marín, Ó. Reinoso, Design of compact switchable magnetic grippers for the HyReCRo structure-climbing robot, *Mechatronics* 59 (2019) 199–212, <https://doi.org/10.1016/j.mechatronics.2019.04.007>.
- [43] P. Ward, D. Liu, K. Waldron, M. Hasan, Optimal design of a magnetic adhesion for climbing robots, *Nat. Inspired Mobile Robot.* (2013) 375–382, https://doi.org/10.1142/9789814525534_0048.
- [44] N. Jinqiang, T. Chaoyang, L. Yuxiang, Inchworm inspired pneumatic soft robot based on friction hysteresis, *J. Robot. Autom.* 1 (2017) 54–63, <https://doi.org/10.36959/673/355>.
- [45] F. Moreira, A. Abundis, M. Aguirre, J. Castillo, P.A. Bhounsule, An inchworm-inspired robot based on modular body, electronics and passive friction pads performing the two-anchor crawl gait, *J. Bionic Eng.* 15 (2018) 820–826, <https://doi.org/10.1007/s42235-018-0069-x>.